Journal Name

ARTICLE TYPE

Cite this: DOI: 10.1039/xxxxxxxxxx

Molecule formation induced by non-uniform plume-air interactions in laser induced plasma†

Pengxu Ran,[a] Huaming Hou,*[ab] and Sheng-Nian Luo[ab]

Received Date
Accepted Date

DOI: 10.1039/xxxxxxxxxx

www.rsc.org/journalname

Measurements with Laser Ablation Molecular Isotopic Spectrometry (LAMIS) are usually performed in atmosphere for rapid isotope analysis, and understanding of molecule formation via plasma-air chemical reactions is important for quantitative analysis of LAMIS. In this work, the expansion of plasma plume from ablation of pure aluminum in air is studied with time- and space-resolved monochromatic imaging and emission spectroscopy. The distributions of neutral Al and O atoms, and AlO radicals formed through plasma chemical reactions are characterized. The emission spectra of AlO bands of $B^2\Sigma^+ - X^2\Sigma^+$ system are synthesized, and rotational-vibrational temperature obtained through fitting experimental spectra. Inter-molecular vibrational band interference is well re-constructed, and self-absorption of bandheads, especially for the (0-0) band, is corrected. Interpretation of spatial-temporal evolutions of plasma species and plasma temperature provides insights into the formation mechanism of AlO radicals in laser-induced plasma.

1 Introduction

Laser ablation of solid targets is widely used for chemical analysis.[1] Laser-induced breakdown spectroscopy (LIBS) utilizes laser ablated plasmas as an emission source.[2,3] Elemental analysis is performed via analyzing emission spectra, assuming that the stoichiometry of a plasma is the same as the ablated material, and its performance greatly depends on plasma's properties and the efficiency of plasma emission detection.[4,5] Nowadays, the capability of LIBS has been expanded from elemental analysis to sensing molecular structure[6] through analyzing the emission from molecules that formed through fragmentation of polyatomic clusters, association of neutral atoms, and vaporization of intact molecules from the ablated surface and gas phase combustion of plasma species with surrounding oxidizers.[7–13]

Most LIBS measurements are conducted in air, and the plasma plume-air interaction can result in the deviation of plasma stoichiometry from that of an ablated material. On the other hand, the interaction can be exploited for isotope analysis through analyzing molecular isotopologues formed via chemical reactions between plasma species and air molecules, and this technique is Laser Ablation Molecular Isotopic Spectrometry (LAMIS).[11] Molecules formed through chemical reactions among plasma species can also be used in LAMIS. To date, detection of several isotopes (H, B, C, O, Cl, Sr and Zr) has been demonstrated with LAMIS.[12] Compared to isotope analysis with mass spectrometry, LAMIS has such advantages as rapid response, simplified sample preparation, and allowing for *in situ*, real time or remote analysis, as demonstrated in our previous works.[14,15] However, the formation mechanisms of molecules in plasma plume are not well understood, because laser ablated plasmas are complex and strongly dependent on the nature and pressure of the ambient gas.[16,17] For example, a study of ^{13}C-labeled benzoic[9] showed that the $^{12}C/^{13}C$ ratios derived from C_2 and CN emission exhibit opposite features, and a possible cause is different formation mechanisms of C_2 and CN. Some C_2 molecules are released directly from molecular fragments, whereas CN formation likely involves atomic carbon or species with a single carbon atom.[9] The formation routes of CN also depend on ambient buffer gas, as reported by Sreedhar *et al*.[18] Recently, investigations on metallic monoxides (*e.g.*, ZrO and UO) were conducted for isotope analysis or understanding formation mechanisms of molecules.[14,19]

Emissions from ions, atoms and molecules can be successively detected during the evolution of a laser-induced plasma, and the maximum emission intensity of molecules and atomic species are well separated in time.[20] Molecules tend to form when the plasma cools down, and temperature gradients are present in the plasma.[16,21] Therefore, distribution of molecules is supposed to be inhomogeneous.[22] Moreover, formation of molecules can be influenced by the interaction of plasma plume and ambient gas,[16] especially for those formed through combination of plasma species and ambient gas molecules.[23–26] The spatial distribution of these molecules can be mediated by shock wave.[27] Previous investigations of molecular emission from laser-induced

[a] *The Peac Institute of Multiscale Sciences, Chengdu, Sichuan 610031, P. R. China; E-mail: hmhou@pims.ac.cn*
[b] *Key Laboratory of Advanced Technologies of Materials, Ministry of Education, Southwest Jiaotong University, Chengdu, Sichuan 610031, P. R. China.*

plasmas were mostly performed ignoring the spatial distribution of plasma emission,[20,28] so plasma plume-ambient gas interaction can hardly be revealed. Spatially and temporally resolved spectral analyses of the formation of molecules, including the distribution difference between formed molecules and ionic/atomic species, and its relationship to plasma temperature, are crucial to understanding the formation mechanism of molecules in laser ablated plumes, and for improving the performance in LAMIS or other techniques based on molecular emission.

In this work, we investigate plasma induced from laser ablation of pure aluminum in air. Aluminum is selected because AlO mission is typically intense and the formation mechanism of AlO is still unclear. The expansion and emission of the plasma is monitored with fast monochromatic imaging, and emission spectroscopy are obtained with high spatial and spectral resolutions. The dynamic distributions of AlO radicals, and neutral O and Al atoms are analyzed in detail. The rotational and vibrational bands of AlO, the $B^2\Sigma^+ - X^2\Sigma^+$ system, are simulated. An improved molecular band synthesis and fitting method is proposed, which reproduces well experimental spectra. The interference between different vibrational sequence (*e.g.*, $\Delta v = 0$ and $\Delta v = +1$) is modeled rather than being treated as a noise-like baseline. Rotational temperature and rotational-vibrational temperature are calculated through fitting experimental spectra with synthetic molecular bands. Moreover, the influence of self-absorption of molecular bands on deduced temperatures is considered and a correction procedure is proposed. Rotational temperatures deduced from several methods are compared. Compared with previous investigations of molecule formation in laser induced plasma plume,[20,27] this work is focused on accurate simulation and fitting of single rotational bands, and calculating rotational temperature with the improved algorithm. Our results bear important applications to quantitative analysis of LAMIS. Correlating dynamic distributions of different species in plasma plume to temperature evolution provides insights into the formation of AlO radicals.

2 Experimental setup

A nanosecond Q-switched Nd:YAG laser operated at 1064 nm, with 50 mJ pulse energy and 5 ns pulse duration, is focused with a fused-silica lens ($f = 50$ mm), and incident on the sample surface for plasma ablation; the crater size is about 200 μm. The laser-induced plasma is imaged by two achromatic lens onto the entrance slit of a Czerny-Turner spectrometer (Horiba JY 1250 M) coupled with an intensified charge-coupled device (ICCD, Andor DH334T-18U-73) detector. The slit is aligned with the plasma center, which is imaged at the center of an ICCD image plane. Prior to being focused, the laser beam is precisely aligned to be parallel to the spectrometer slit. A grating with 2400 g/mm is used to capture spectra with a resolution of about 20 pm over all the spectral range investigated. It enables an accurate measurement of the AlO rotational lines. A grating with 1200 g/mm is used to capture the spectra of neutral oxygen emissions. The ICCD is operated at the image mode and each 2D spectrum represents the integration of 15 laser shots. Wavelength calibration is performed by recording Fe lines emitted from very late time laser induced plasmas from pure iron samples. The Stark shifts of Fe lines are negligible, as confirmed by comparing the spectra from a plasma and a hollow cathode iron lamp. The spectral response and sensitivity of the entire optical system are calibrated as follows. A certified blackbody light source is placed at a plasma source under consideration, and its spectrum is captured with the spectrum detection system identical to that for the plasma source. Calibration is done via comparing plasma source spectral intensity (after background substraction) with that of the certified light source.

A pair of achromatic lenses (BK7) are used to image plasma directly onto another ICCD camera, along the axis perpendicular to both the laser beam and the optical path of the spectrometer system. Spectroscopically resolved images for different species in the plasma plume are obtained with narrow band filters with transmission wavelengths corresponding to characteristic lines of certain species, such as AlO radicals and neutral Al and O atoms. Each image is the accumulation of 5 acquisitions. The ICCD dark current is subtracted from spectroscopic images and direct images. The plasma emission spectra and images are temporally resolved via triggering ICCD at different delay times. The laser and two ICCDs are controlled by a pulse generator DG535 from Stanford Research Systems. The magnifications of the two systems are calibrated with a reticle.

3 Results and discussion

3.1 Monochromatic imaging of plasma expansion

Laser ablated sample materials and dissociated air molecules constitute a plasma plume. Intense emission from neutral Al and O atoms as well as AlO radicals dominates the spectrum. Distributions of each species at different stages of plasma evolution are studied by monochromatic imaging with bandpass filters. Three bandpass filters from Thorlabs, FB390-10, FL488-10 and FL780-10, are used for imaging Al atoms, AlO molecules and O atoms, respectively. All the three bandpass filters feature 10±2 nm FWHM with their central wavelengths located near the peak of the atomic lines and bandhead of molecular bands. Fig. 1 shows the distribution of excited AlO, Al and O species in the plasma at various times during plasma evolution. The images of these three species (AlO, Al and O) are displayed in different false colors, with red for AlO radicals ((0-0) band of the $B^2\Sigma^+ - X^2\Sigma^+$ system), green for neutral aluminum (Al I 394.4 nm and 396.15 nm), and blue for neutral oxygen (O I 777.2 nm). Here, the Al I lines used for imaging may suffer from self-absorption, leading to slight deviation of the observed distribution of aluminum atoms from the real distribution, especially for the inner part of plasma. However, the influence is negligible for comparison of distributions of different species. To better show plasma structure, each species is normalized to 0–1 based on its own maximum and minimum of intensity.

To minimize the bremsstrahlung radiation component that contributed to the intensity of apparent images of AlO at early time (≤ 2 μs), the emission existence of AlO radicals is confirmed firstly by measuring the axially resolved spectrum of AlO (0-0) band with the same gating time simultaneously, and then the ax-

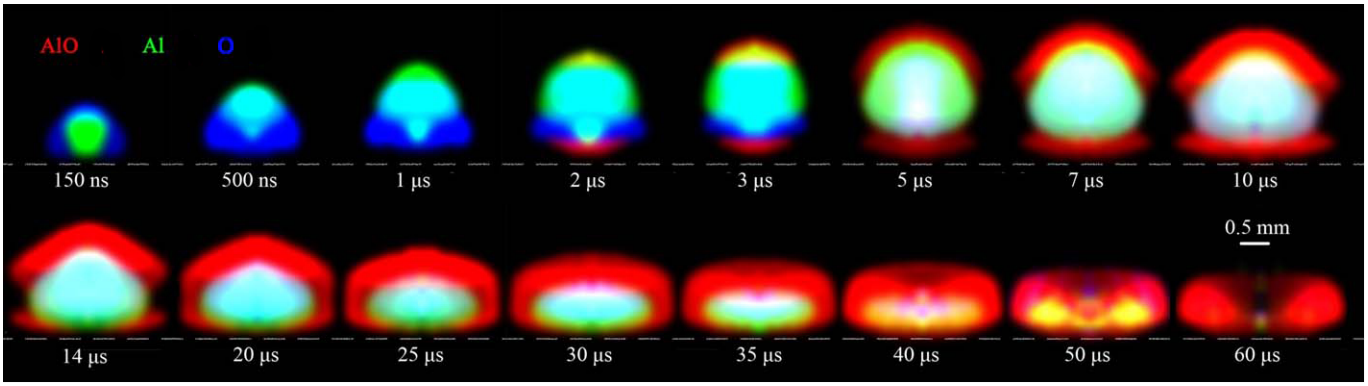

Fig. 1 Time-resolved spectroscopic images of neutral Al and O atoms and excited AlO radicals in an Al plasma at atmospheric pressure induced with a laser pulse energy of 50 mJ (fluence of 160 J/cm^2). For recording these images, three different narrow band-pass filters with transmission centered at 488 nm (AlO), 780 nm (O) and 390 nm (Al) are used. False colors are used to represent the three different species in the plume with red for AlO radicals, green for neutral Al atoms and blue for neutral O atoms. The emission intensity of each species is normalized to 0-1 based on its own maximum and minimum. The dash lines represent the sample surface.

ial intensities of AlO bandhead are corrected by subtracting the continuum baseline near bandhead from spectrum of AlO bands. The focusing lens is well aligned to ensure that the laser ablated plasmas are rotationally symmetric. The Abel inversion is then applied to each image, yielding spatial intensity distribution of each species.[29] Prior to the inverse Abel transformation, the 2D images are smoothed with the Savitzky-Golay filter to reduce random noise.

As early as 150 ns, Al and O species show a layered structure. The spherical plasma morphology and such layered structure correspond to the consequence of laser-induced detonation wave.[30,31] The excited aluminum plume is enclosed by O atoms. Strong emission of O is visible, indicating the abundance of neutral O atoms in the plasma. Afterwards (0.5 to 1 μs), the aluminum plume penetrates into surrounding air from the top, resulting in mixing of Al and O atoms at the central part of the plasma. Meanwhile, a zone rich in neutral O atoms is observed at the bottom. To the contrary, AlO radicals appear first at the bottom other than at the top, even though the neutral Al atoms are enriched at the top. A possible cause is the flow of cold ambient air molecules into the gap between plasma plume and sample surface, and further diffuse into the plasma plume, due to the vorticity generated by the initially non-spherical shock wave.[27,32] The fast cooling of plasma promotes the association of neutral Al and O atoms and combustion of Al species with air molecules. At 3 μs, distinct AlO emission at the top of plasma shows a spherical layered structure expanding towards sample surface along the periphery of plasma. This agrees well with theoretically predicted phenomenon that chemical bonding occurs only in a boundary layer of the plume with a high temperature gradient, as reported by Shabanov *et al.*[33] Such an expansion leads to plasma cool down and size reduction (see details in section 3.3). At later delays after 40 μs, the emissions of both neutral Al atoms and AlO radicals reach a maximum at the radial position of ~0.6 mm and decrease to zero at plume center, giving rise to a donut-like emission structure. At a delay time of 500 ns−5 μs, a green spherical layer at plasma border indicates that oxygen emission in this area is pretty weak, other than that aluminum emission in this area is stronger than the emission in the central part of plasma. The light blue area merges Al (green) and O (blue).

3.2 Axial emissions profiles of neutral Al, O atoms and AlO radicals

To further characterize the plasma, we present in Fig. 2 normalized axial profiles of integrated emission intensity for neutral Al and O atoms. For O atoms, O 777.2 nm (with lower energy level of 9.1 eV) is chosen to circumvent self-absorption. For Al atoms, the resonance line (Al 396.2 nm) is chosen because of its long persistent time and high signal-to-noise ratio. In addition, our detector is not sensitive to Al atomic lines located in the UV range. Self-absorption of this line is examined via analyzing the recorded spectra. For short delays (< 3 μs), self-absorption is negligible due to the high degree of ionization of the Al vapor. In order to minimize the influence of self-absorption, we use the integrated line intensity (Fig. 2). The axial position (z) represents the vertical distance with respect to the sample surface ($z = 0$). The gate width of the ICCD is different for different gate delay time, and all the spectra are normalized to the ICCD gate width (in unit of 1 μs). To enhance the signal-to-noise ratio, averaging over 15 ablation shots is adopted, and each spectrum measurement is repeated five times to compensate for the lower signal-to-noise ratio.

The emissions from neutral Al atoms and O atoms are originated from the target and ambient air, respectively. Both distributions of neutral O and Al atoms become spread out initially ($t < 5$ μs). However, emission zones for species from the target and ambient air are considerably different. First, the intensity peak of neutral Al atoms moves from $z \sim 0.5$ mm at $t = 0.15$ μs to 1.2 mm at 5 μs, whereas that for neutral O atoms tends to remain around $z \leq 0.5$ mm for all delay times. Second, during plasma expansion, the front edge of the Al emission zone is outside the O zone. One possible reason is that the excitation energy level for O I 777.2 nm (10.7 eV) is much higher than that of Al I 394.4 nm (3.1 eV), and the temperature in the periphery is typically much lower than in the central core.[16] As a result, much higher percent-

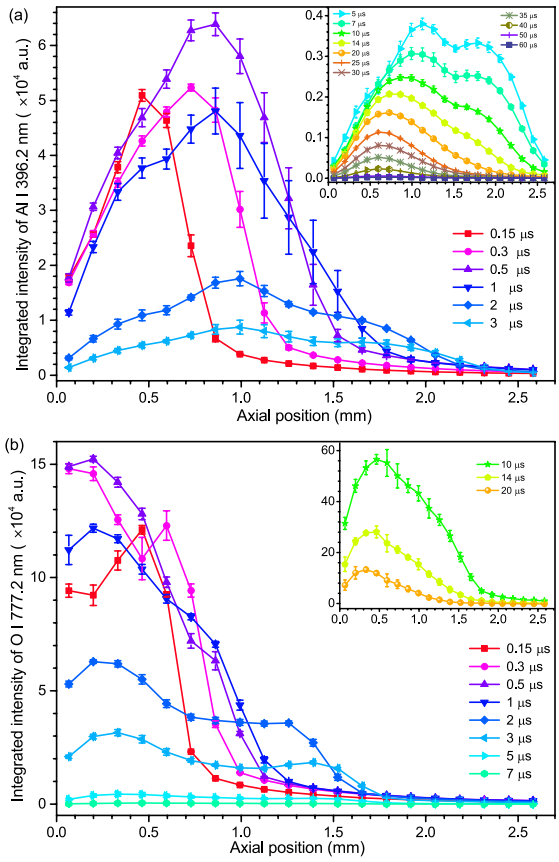

Fig. 2 Time-resolved emission intensity as a function of axial distance for (a) neutral Al atoms (Al I 396.2 nm) from the target and (b) neutral O atoms (O I 777.2 nm) from air. The intensity profiles with longer delay time are shown in insets.

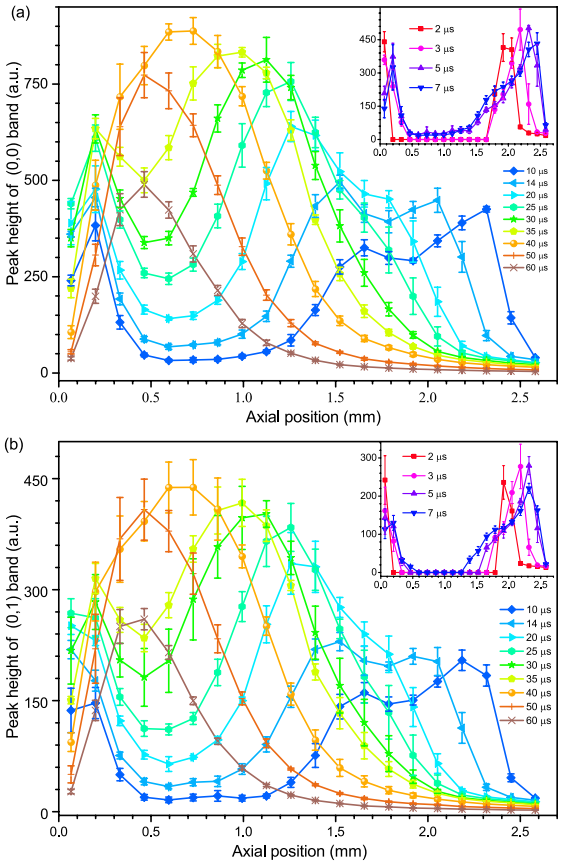

Fig. 3 Time-resolved emission intensity of (a) (0,0) band and (b) (0,1) band of $B^2\Sigma^+ - X^2\Sigma^+$ system as a function of axial distance for AlO radicals formed through plasma chemical reaction. The intensity profiles with short delay time (less than 7 μs) are shown in insets.

age of O atoms populate at ground energy level and O atoms in the periphery cannot be detected via emission imaging. However, plasma cooling facilitates the formation of AlO molecules.

For AlO radicals, the temporal-spatial evolutions of the band-head intensities for the (0-0) and (0-1) bands of the $B^2\Sigma^+ - X^2\Sigma^+$ system are shown in Fig. 3a and b, respectively, and different from those for neutral O and Al atoms. The AlO emission can only be observed at delays beyond 2 μs. For delays between 2 and 7 μs, AlO emission is only observed at the very top and bottom of plasma plumes, and AlO emission is hardly detectable from the central part, whereas the emissions of both neutral O and Al atoms are relatively strong.

The formation mechanisms of AlO include dissociation of free O and Al atoms and combustion of free Al atoms with O_2 from air when plasma cools down.[20,27] Interaction of plasma plume with air through thermal conduction and mixing is the dominant mechanism for plasma cooling. Plasma-air interaction mainly occurs at the top of a plasma plume during plasma expansion, although this expansion is nearly spherical (Fig. 1). Another significant difference is that the AlO emission zone at the top of the plume expands towards lower axial positions with evident intensity enhancement before the final decay at delay time of about 40 μs, but the evolution of emission intensity of AlO from the bottom of plasma zone is moderate both in time and along the axis. The formation of AlO radicals is closely linked to plasma temperature and its distribution, because plasma chemical reactions are thermally dependent, and ionization of atoms and molecules may further mediate chemical dissociation and association.[33] Further cooling down of plasma will lead to intensity decay of AlO molecular bands because the population degeneration of AlO molecules in an excited state. Moreover, at lower temperatures, AlO molecules can further react with oxygen through reactions:[34] $AlO + O_2 \rightarrow AlO_2 + O$ and $AlO + AlO_2 \rightarrow Al_2O_3$, which result in a decrease of AlO density. Formation of polyatomic molecules would deplete the population of diatomic molecules, as reported by Hartig *et al.*[19] in their study of evolution of UO molecules in laser-induced plasma.

3.3 Rotational and vibrational temperature analysis

3.3.1 Simulation of AlO $B^2\Sigma^+ - X^2\Sigma^+$ band spectra

Emission spectra of AlO radicals were thoroughly studied and several advanced spectrum simulation algorithms were recently developed.[35–37] Rotational and vibrational temperatures of molecules can be determined by comparison of an experimental band spectrum with its corresponding synthetic spectrum. If we assume that plasma is under local thermodynamic equilibrium

(LTE), the emission intensity of a molecular band is given by[38]

$$I_{n',n'',v',v'',J',J''} = C_e \frac{q_{v',v''} S_{J',J''}}{Q_{rot} v'} (\nu_{J',J''})^4 \exp\left\{\frac{-G(v)hc}{kT_{vib}}\right\} \exp\left\{\frac{-F(J)hc}{kT_{rot}}\right\} \quad (1)$$

Here, h is Plank's constant, k is Boltzmann's constant, C_e is emission constant, and n is the principle quantum number, $\nu_{J',J''}$ is the transition wavenumber. T_{vib} and T_{rot} are the vibrational and rotational temperatures, respectively. Q_{rot} is the rotational partition function, $S_{J',J''}$ is Hönl-London factors and $q_{v',v''}$ is the Frank-Condon coefficient. $G(v)$ and $F(J)$ are the vibrational and rotational energy terms, respectively.

In this study, the AlO blue-green B-X system observed has a relatively large transition probability. The molecular band comprises two principal branches (R and P) and additional branches (Q) with significantly lower intensity. In this paper, the ExoMol database[39] is used in the simulation, which provides a more accurate line position with respect to that calculated with molecular constants,[40] especially for rotational lines with high J numbers. The simulation approach of molecular bands is similar to previous works[14,15] but with modifications. The $B^2\Sigma^+ - X^2\Sigma^+$ bands are red-degraded, and high J-lines contribute to form a quasi-continuum extending widely in the red part of each individual band. The overlaps of lines from the Δv and $\Delta v + 1$ vibrational sequences are considered. For example, rotational lines with high J numbers from the $\Delta v + 1$ vibrational sequence underlie those from the Δv vibrational sequence. In previous studies, the interfering lines were not analyzed in detail via comparing experimental and high resolution synthetic spectra.

Thus, the simulation was performed by four parameters: the emission constants ($C_{\Delta v}$ and $C_{\Delta v+1}$), temperature (T), apparatus peak broadening ($\Delta\lambda$). The temperature information of plasma is extracted by fitting the data with synthetic emission spectra. The fitting algorithm locates the best combination of all fitting parameters by minimization of the sum of squares of the fitting residuals ($\varepsilon(\lambda)$) at all wavelength (λ) of the experimental spectrum (I^{expt}_{AlO}) through

$$I^{expt}_{AlO}(\lambda) = I^{syn}_{AlO-C_{\Delta v}}(C_{\Delta v}, \lambda, T, \Delta\lambda) + I^{syn}_{AlO-C_{\Delta v+1}}(C_{\Delta v+1}, \lambda, T, \Delta\lambda) + I_{continuum} + \varepsilon(\lambda) \quad (2)$$

Here we note that intensities $I^{syn}_{AlO-C_{\Delta v}}$ and $I^{syn}_{AlO-C_{\Delta v+1}}$ are assigned with two different fitting coefficients, in order to account for possible difference in vibrational temperature and deviations from equilibrium in laser-induced plasma. In our experiments, a spectrograph with a very high spectral resolution is used, and each spectrum only covers two neighboring vibrational bands, so the rotational temperature and vibrational temperatures are assumed to be the same ($T_{rot} = T_{vib} = T$).

Two typical experimental spectra of the AlO $B^2\Sigma^+ - X^2\Sigma^+$ $\Delta v = 0$ and $\Delta v = -1$ vibrational sequences together with their fittings are shown in Fig. 4a and b, respectively. For better fitting of interference lines, the bandheads of (0-0) and (0-1) are located at the center of spectrum detection window, and as a result, the neighboring molecular bands, for instance, (1-1) and (1-2), are not covered. The spectrometer measures emission from the very top of a plasma, and self-absorption should be negligible because the radial optical absorption length is very short, and lower number density of AlO molecules in the $X^2\Sigma^+$ state is expected as AlO molecules further react with oxygen from air. As seen from Fig. 4, even the noise-like baseline can be well fitted with simulated band spectra for both molecular bands. Moreover, the noise-like baseline can be further re-constructed. For example, the baseline shown in Fig. 4a consists of the rotational lines with high J numbers from vibrational bands, (1-0), (2-1), (3-2), (4-3) and (5-4).

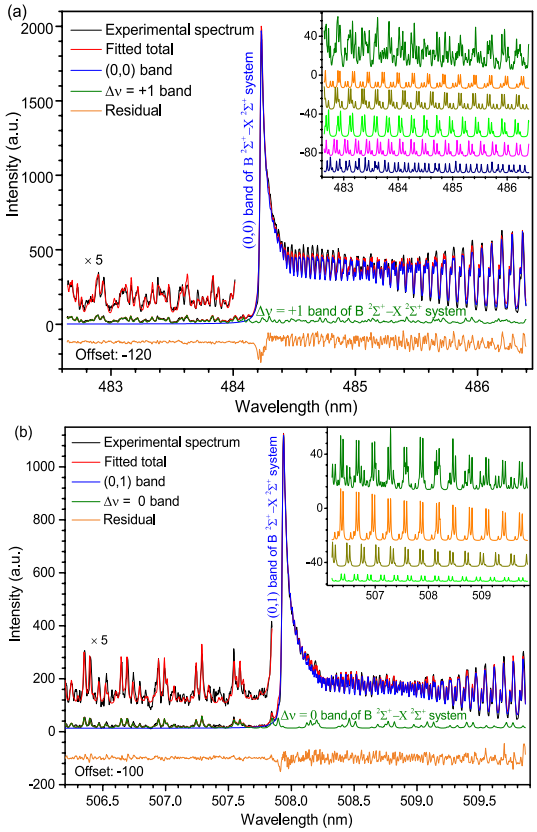

Fig. 4 Typical experimental spectra (black) of (0-0) and (0-1) bands of $B^2\Sigma^+ - X^2\Sigma^+$ system together with their corresponding fittings (red). Spectra are acquired from the very top of plasma at a delay time of 30 μs. Each single rotational band is further re-constructed through the fitting procedure. The spectrum in olive is the sum of the re-constructed band tails of $\Delta v = +1$ band (a) and $\Delta v = 0$ band (b) of $B^2\Sigma^+ - X^2\Sigma^+$ system. The spectrum in blue is the re-constructed (0-0) band (a) or (0-1) band (b) of $B^2\Sigma^+ - X^2\Sigma^+$ system. The six spectra shown in insert of figure (a) from top to bottom are the sum of re-constructed band tails of $\Delta v = +1$ vibrational sequence and single rotational band of (1-0), (2-1), (3-2), (4-3) and (5-4), respectively. The four spectra shown in inset of (b) from top to bottom are the sum of re-constructed band tails of $\Delta v = 0$ vibrational sequence and single rotational band of (0-0), (1-1) and (2-2), respectively. The fitting residuals were shown at bottom of each figure with offset.

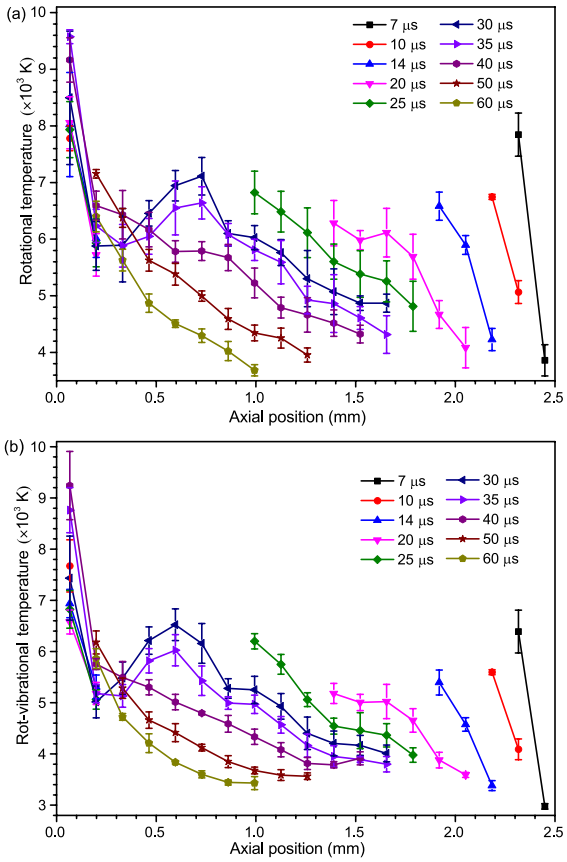

Fig. 5 Axial profiles of rotational temperature and rot-vibrational temperature for delays from 7 to 60 μs. Rotational temperature is deduced through fitting (0-1) band of $B^2\Sigma^+ - X^2\Sigma^+$ system in the spectral range from 507.67 to 510.10 nm, and rot-vibrational temperature is deduced via fitting (0-1) and (1-2) bands of $B^2\Sigma^+ - X^2\Sigma^+$ system in the spectral range from 507.67 to 511.39 nm.

3.3.2 Spatio-temporal evolution of the plasma temperature

Using the method introduced above, we obtain temporal-spatial evolutions of rotational (T_{rot}) and rotational-vibrational temperature ($T_{\mathrm{rot-vib}}$) from 7 to 60 μs (Fig. 5). T_{rot} and $T_{\mathrm{rot-vib}}$ are deduced via fitting the (0-1) band in the spectral range of 507.67–510.10 nm, and both (0-1) and (1-2) bands in the range of 507.67–511.39 nm, respectively. Here the $\Delta v = -1$ vibrational sequence is used to reduce the error due to self-absorption. The temperature profiles of T_{rot} and $T_{\mathrm{rot-vib}}$ at the same delay time are quite similar, but $T_{\mathrm{rot-vib}}$ is slightly lower than T_{rot}.

The vibrational and rotational temperature both describe the population of energy levels in molecular species. The vibrational energy levels are given by a pure Boltzmann distribution, but the thermal population of rotational energy levels is the product of the Boltzmann factor and the fold degeneracy. Moreover, for molecules formed at spherical zone of plasma, collisions between heavy particles are the predominant mechanism of thermalization,indicating a deviation from a local thermodynamic equilibrium. Lower vibrational temperature is typically observed at late stage of plasma evolution, similar to the case of C_2 and TiO molecules.[26,41] Because the electron density is much lower than that of heavy particles.[26] The excitation state of AlO radicals can also be mediated by chemical reactions, since reaction $Al + O_2 \rightarrow AlO(X^2\Sigma^+) + O$ is almost isoenergetic,[42] the AlO $(B^2\Sigma^+)$ state can hardly be produced via single-collision events.[43] Instead, the reaction sequence $Al + O + O_2 \rightarrow AlO_3$, and $AlO_3 \rightarrow AlO(B^2\Sigma^+) + O_2$ was proposed[44] for the formation of the $B^2\Sigma^+$ state.

Due to plasma expansion, and the interaction of plasma plume with ambient air, temperature is lower in the periphery zone than that in the centre of plasma. As a result, the AlO radicals is enriched in the periphery of a plasma especially at later stages, since its number density decreases exponentially with increasing temperature (for $T > 3000$ K), according to previous calculations.[37] Harilal *et al*.[27] also reported that AlO/Al ratio increased greatly whilst plasma temperature dropped from 5000 K to 3000 K. This is consistent with the image sequence shown in Fig. 1. Moreover, the temperature remains higher at lower axial positions during the whole process, where O atoms are enriched (Fig. 2b), because higher temperature is necessary to populate the O atoms in an excited state. However, Al atoms tend to become ionized at elevated temperatures.[37]

3.3.3 Self-absorption correction of simulated molecular spectra of (0-0) bands

Utilization of molecular emission for integral plasma temperature measurements was previously reported.[22] However, the most intense (0-0) band typically suffers self-absorption,[45] which may result in deviation between simulated and measured spectra, especially for bandheads. Two models for self-absorption correction have been reported. In one model, laser-induced plasma is approximated by a hemispherical shape and divided into two zones (the plasma core and the peripheral zone) with different temperatures.[37] However, for laser-induced aluminum plasma in this study, most AlO molecules form at the peripheral zone (Fig. 1) and molecular emissions from the plasma core is relatively weak, and can be ignored. Thus, a homogeneous peripheral media without temperature or density gradients for the emission and absorption is assumed, and AlO radicals in the excited state and ground state co-exist and in thermal equilibrium.

The intensity of emission from a homogeneous media is given by[46]

$$I(\nu) = \frac{\varepsilon(\nu)}{\kappa(\nu)}\left\{1 - \exp\left[-\kappa(\nu)L\right]\right\} \tag{3}$$

Here $\varepsilon(\nu)$ and $\kappa(\nu)$ are the emission and absorption coefficients, respectively, and L is the geometrical thickness of the emission region. For simulated spectrum ($I^{\mathrm{syn}}_{\mathrm{AlO}}$), the self-absorption is zero, and $I^{\mathrm{syn}}_{\mathrm{AlO}} = \varepsilon(\nu)L$. Since $\varepsilon(\nu) = \alpha\rho(\nu,T)\kappa(\nu)$, Eq (3) can be rewritten as

$$I(\nu) = \alpha\rho(\nu,T)\left\{1 - \exp\left[-\frac{I^{\mathrm{syn}}_{\mathrm{AlO}}}{\alpha\rho(\nu,T)}\right]\right\} \tag{4}$$

where $\rho(\nu,T) = 2h\nu^3/c^2/\left(e^{h\nu/kT} - 1\right)$ and α is a fitting parameter. $I(\nu)$ is experimental spectrum. For the fitting process with self-absorption correction, $I^{\mathrm{syn}}_{\mathrm{AlO}-C_{\Delta v+1}}$ and $I^{\mathrm{syn}}_{\mathrm{AlO}-C_{\Delta v}}$ are first obtained via fitting without self-absorption correction, through

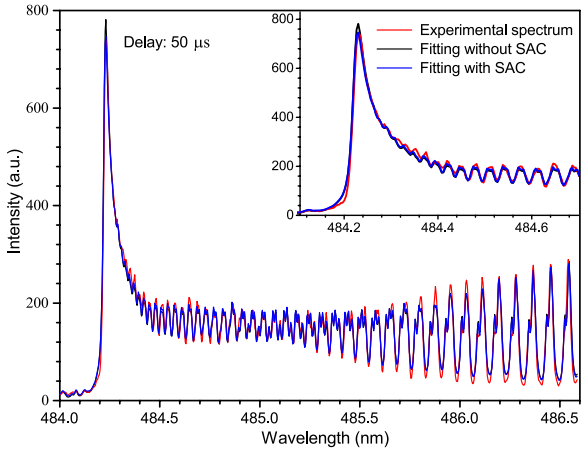

Fig. 6 Experimental spectrum and synthetic spectra with and without self-absorption correction (SAC). The spectrum is acquired at a delay time of 50 μs and an axial distance of 0.6 mm. The inset shows the bandhead of (0-0) band of $B^2\Sigma^+ - X^2\Sigma^+$ system.

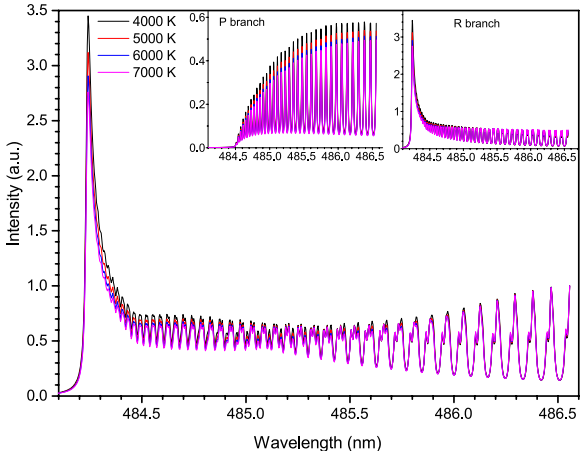

Fig. 7 Simulated (0-0) band of AlO $B^2\Sigma^+ - X^2\Sigma^+$ system at temperature of 4000, 5000, 6000 and 7000 K. All spectra are scaled to the same maximum and minimum at 486.4–486.6 nm. The components of P and R branches are shown separately in insets.

$$I_{\mathrm{AlO}}^{\mathrm{expt}}(\lambda) = \eta I_{\mathrm{AlO-C}_{\Delta v+1}}^{syn} + \xi I_{\mathrm{AlO-C}_{\Delta v}}^{syn} + \delta(v) \tag{5}$$

$\delta(v)$ is the fitting residual, η and ξ are fitting coefficients. Afterwards, $\eta I_{\mathrm{AlO-C}_{\Delta v+1}}^{syn}$ is subtracted from experimental spectrum, $I_{\mathrm{AlO}}^{\mathrm{expt}}(\lambda)$, for further fitting with self-absorption correction algorithm, through

$$I_{\mathrm{AlO}}^{\mathrm{expt}}(\lambda) - \eta I_{\mathrm{AlO-C}_{\Delta v+1}}^{syn} = \alpha\rho(v,T)\left\{1 - \exp\left[-\frac{\xi I_{\mathrm{AlO-C}_{\Delta v}}^{\mathrm{syn}}}{\alpha\rho(v,\mathrm{T})}\right]\right\} + \varepsilon(v) \tag{6}$$

Here $\varepsilon(v)$ is the fitting residual.

The self-absorption correction algorithm is applied to AlO (0-0) band spectrum fitting in the spectral range from 484.0 to 486.6 nm. An improved fitting accuracy is obtained as demonstrated in Fig. 6. The bandhead intensity deviation from experimental spectrum is about 6% for the fitting without self-absorption correction, and reduced to 1% with the self-absorption correction.

An alternative method to minimize the effect of self-absorption on deduced temperature is fitting a molecular spectrum without its bandhead.[45,47] However, for AlO $B^2\Sigma^+ - X^2\Sigma^+$ (0-0) band, our simulation (Fig. 7) reveals that the rotational temperature can hardly be precisely deduced from the well-separated rotational lines located near the bandhead of $B^2\Sigma^+ - X^2\Sigma^+$ (1-1) (*e.g.*, 485.5–486.3 nm), because the relative intensity ratios among these lines are weakly temperature dependent. This is reasonable because upper energy levels of these rotational transitions are very close. Due to the high resolution spectrography used in this experiment, the well separated rotational lines can extend to as low as 484.5 nm.

The temperatures are obtained with three different fitting algorithms as introduced above. The spatial temperature profiles presented for $t = 40$ and 50 μs (Fig. 8) are similar to those in Fig. 5. The temperatures calculated through fitting experimental spectra with synthetic spectra are evidently higher. This is reasonable because the apparent bandhead intensity is suppressed due to the self-absorption effect. The bandhead consists of R branch rotational lines with low J numbers. The temperatures deduced through fitting molecular bands without bandhead is quite similar to that deduced via fitting the whole rotational band with self-absorption corrected synthetic spectra.

Thus, these two methods can be used for temperature analysis using molecular bands with self-absorption. The temperatures deduced from the (0,0) band (Fig. 8) with self-absorption correction are slightly higher (about 10%−20%) than those from the (0,1) band (Fig. 5a), although they should be same because the upper energy levels for these two rotational bands are identical. The possible reason is the precision of Hönl-London factors and the error of spectral response calibration of our detection system, since the upper energy levels of the rotational lines are very close (< 0.37 eV), and temperature is very sensitive to the relative intensity among rotational lines.

The knowledge on AlO and temperature distributions, together with their evolutions, allows one to analyze plasma characteristics. Such analysis reveals that plasma can hardly reach a homogeneous state because AlO molecules are always enriched in the periphery of a plasma plume, even at very late stages of plasma evolution. This agrees well with previous studies.[22] The temperature deduced from molecular spectra is not comparable to that calculated from atomic or ionic lines, because different species (molecules vs atoms and ions) concentrate in different zones of a plasma plume. For molecular analysis, a complete thermal equilibrium state of a whole plasma plume can hardly be assumed because the temperature deviation over axial position can be up to about 2000 K (Fig. 5). Chemical analysis (*e.g.*, LAMIS) with molecular spectra emitted from a small portion of a plasma and spectrum acquisition with a narrow gate are encouraged to reduce the errors induced by the inherent inhomogeneity of a plasma plume.

The temperature analysis in this work is focused on rotational temperature, which is considered very important for LAMIS analysis. The formation of AlO radicals is attributed to plasma cooling, which facilitates the association of free neutral O and Al atoms

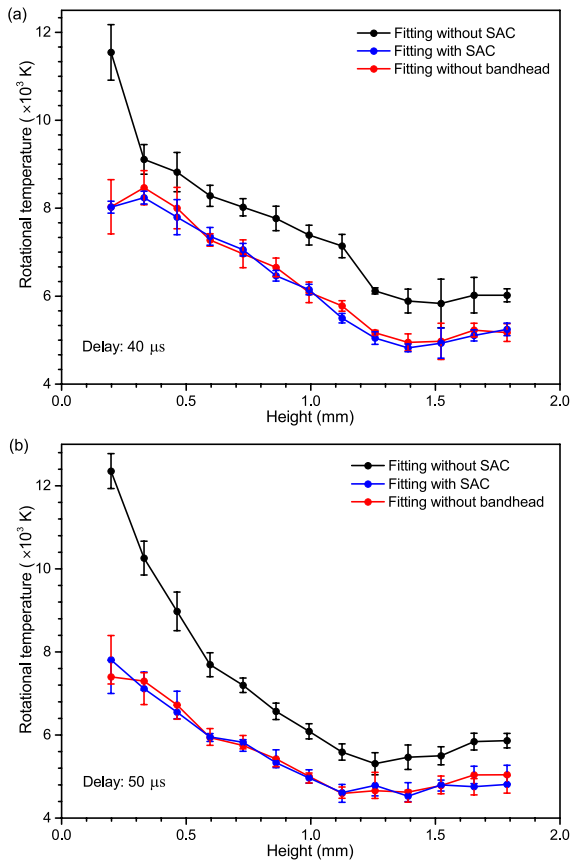

Fig. 8 Rotational temperature as a function of axial position. Temperature is obtained through fitting experimental spectra with synthesized molecular spectra and self-absorption corrected band spectra, and fitting spectra without bandhead. (0-0) band of AlO $B^2\Sigma^+ - X^2\Sigma^+$ system is used here. For fitting without bandhead, the spectra in the range of 484.5 to 486.3 nm are used.

and combustion of Al species with O_2 in ambient air. Although the number density of each species of homogeneous plasma in LTE can be roughly estimated,[27,37] the dominant mechanisms remain to be resolved, because the product is the same (AlO radicals) and the reactants are mixed. Moreover, some of the intermediate products[42] (*e.g.*, OAlO and AlOAlO) are not detectable at present. Isotopic labeling of sample or ambient gas in conjunction with LAMIS can potentially differentiate such products. For example, isotope labeled $Al_2{}^{18}O_3$ can be used as sample and the products from association ($Al^{18}O$ radicals) and combusting ($Al^{16}O$) can be well resolved by analyzing spatial-temporal evolutions of emission. The isotope shift is about 1 nm for the (0-1) bandhead of AlO $B^2\Sigma^+ - X^2\Sigma^+$ system, which is sufficient for quantitative analysis of molecular isotopologues.[12]

4 Conclusions

The spatial and temporal evolutions of laser-induced plasma from a pure aluminum target in air are investigated with monochromatic imaging and emission spectroscopy. The AlO radicals are mainly situated outside the aluminum and oxygen plume, as confirmed by the axial profiles of emissions from neutral Al and O atoms, and AlO radicals, indicating non-uniformity of the plasma plume.

The rotational-vibrational molecular bands of AlO $B^2\Sigma^+ - X^2\Sigma^+$ system are theoretically synthesized and further used for plasma temperature calculation via fitting experimental spectra. The interference between vibrational bands is well demonstrated in simulated and experimental spectra. A self-absorption correction algorithm is employed for rotational temperature determination with the (0-0) band, and the deduced temperature agrees well with that calculated through fitting the rotational bands without bandhead. Knowledge on spatial and temporal evolution of AlO allows one to perform accurate plasma temperature analysis.

Acknowledgments

The research was supported by National Science Foundation of China (No. 61605161), Science Challenge Project (No. TZ2016001), and the Fundamental Research Funds for the Central Universities (No. 2682017CX074). We thank Dr. Xianglei Mao for helpful discussion about molecular band simulation.

References

1 R. E. Russo, X. Mao, J. J. Gonzalez, V. Zorba and J. Yoo, Anal. Chem., 2013, **85**, 6162–6177.
2 F. J. Fortes, J. Moros, P. Lucena, L. M. Cabalín and J. J. Laserna, Anal. Chem., 2012, **85**, 640–669.
3 N. H. Bings, A. Bogaerts and J. A. Broekaert, Anal. Chem., 2010, **82**, 4653–4681.
4 E. Tognoni, G. Cristoforetti, S. Legnaioli and V. Palleschi, Spectrochim. Acta Part B, 2010, **65**, 1–14.
5 J. Aguilera and C. Aragón, Spectrochim. Acta Part B, 2007, **62**, 378–385.
6 J. Serrano, J. Moros and J. J. Laserna, Anal. Chem., 2015, **87**, 2794–2801.
7 F. Nakadi, M. da Veiga, M. Aramendía, E. Garcia-Ruiz and M. Resano, J. Anal. At. Spectrom., 2015, **30**, 1531–1540.
8 J. Serrano, J. Moros and J. J. Laserna, J. Anal. At. Spectrom., 2015, **30**, 2343–2352.
9 M. Dong, G. C.-Y. Chan, X. Mao, J. J. Gonzalez, J. Lu and R. E. Russo, Spectrochim. Acta Part B, 2014, **100**, 62–69.
10 R. Glaus, J. Riedel and I. Gornushkin, Anal. Chem., 2015, **87**, 10131–10137.
11 R. E. Russo, A. A. Bol'shakov, X. Mao, C. P. McKay, D. L. Perry and O. Sorkhabi, Spectrochim. Acta Part B, 2011, **66**, 99–104.
12 A. A. Bol'shakov, X. Mao, J. J. González and R. E. Russo, J. Anal. At. Spectrom., 2016, **31**, 119–134.
13 X. Mao, A. A. Bol'shakov, D. L. Perry, O. Sorkhabi and R. E. Russo, Spectrochim. Acta Part B, 2011, **66**, 604–609.
14 H. Hou, G. C.-Y. Chan, X. Mao, V. Zorba, R. Zheng and R. E. Russo, Anal. Chem., 2015, **87**, 4788–4796.
15 H. Hou, G. C.-Y. Chan, X. Mao, R. Zheng, V. Zorba and R. E. Russo, Spectrochim. Acta Part B, 2015, **113**, 113–118.
16 Q. Ma, V. Motto-Ros, W. Lei, M. Boueri, X. Bai, L. Zheng, H. Zeng and J. Yu, Spectrochim. Acta Part B, 2010, **65**, 896–907.

17 X. Bai, F. Cao, V. Motto-Ros, Q. Ma, Y. Chen and J. Yu, Spectrochim. Acta Part B, 2015, **113**, 158–166.

18 S. Sreedhar, E. N. Rao, G. M. Kumar, S. P. Tewari and S. V. Rao, Spectrochimica Acta Part B: Atomic Spectroscopy, 2013, **87**, 121–129.

19 K. C. Hartig, S. S. Harilal, M. C. Phillips, B. E. Brumfield and I. Jovanovic, Optics Express, 2017, **25**, 11477–11490.

20 X. Bai, V. Motto-Ros, W. Lei, L. Zheng and J. Yu, Spectrochim. Acta Part B, 2014, **99**, 193–200.

21 G. Cristoforetti, E. Tognoni and L. Gizzi, Spectrochim. Acta Part B, 2013, **90**, 1–22.

22 J. Lam, V. Motto-Ros, D. Misiak, C. Dujardin, G. Ledoux and D. Amans, Spectrochim. Acta Part B, 2014, **101**, 86–92.

23 B. Yee, K. Hartig, P. Ko, J. McNutt and I. Jovanovic, Spectrochim. Acta Part B, 2013, **79**, 72–76.

24 X. Mao, A. A. Bol'shakov, I. Choi, C. P. McKay, D. L. Perry, O. Sorkhabi and R. E. Russo, Spectrochim. Acta Part B, 2011, **66**, 767–775.

25 C. Koral, A. De Giacomo, X. Mao, V. Zorba and R. E. Russo, Spectrochim. Acta Part B, 2016, **125**, 11–17.

26 A. De Giacomo, M. Dell'Aglio, O. De Pascale, R. Gaudiuso, V. Palleschi, C. Parigger and A. Woods, Spectrochim. Acta Part B, 2014, **100**, 180–188.

27 S. S. Harilal, B. E. Brumfield, B. D. Cannon and M. C. Phillips, Anal. Chem., 2016, **88**, 2296–2302.

28 S. S. Harilal, J. Yeak, B. E. Brumfield, J. D. Suter and M. C. Phillips, J. Anal. At. Spectrom., 2016, **31**, 1192–1197.

29 O. Nestor and H. Olsen, SIAM review, 1960, **2**, 200–207.

30 M. Boueri, M. Baudelet, J. Yu, X. Mao, S. S. Mao and R. Russo, Appl. Surf. Sci., 2009, **255**, 9566–9571.

31 S.-B. Wen, X. Mao, R. Greif and R. E. Russo, J. Appl. Phys., 2007, **101**, 023115.

32 H. Sobral, M. Villagrán-Muniz, R. Navarro-González and A. C. Raga, Appl. Phys. Lett., 2000, **77**, 3158–3160.

33 S. Shabanov and I. B. Gornushkin, Applied Physics A, 2015, **121**, 1087–1107.

34 T. N. Piehler, F. C. DeLucia, C. A. Munson, B. E. Homan, A. W. Miziolek and K. L. McNesby, Applied optics, 2005, **44**, 3654–3660.

35 C. G. Parigger and J. O. Hornkohl, Spectrochim. Acta Part A, 2011, **81**, 404–411.

36 C. G. Parigger, A. C. Woods, D. M. Surmick, G. Gautam, M. J. Witte and J. O. Hornkohl, Spectrochim. Acta Part B, 2015, **107**, 132–138.

37 J. Hermann, A. Lorusso, A. Perrone, F. Strafella, C. Dutouquet and B. Torralba, Phys. Rev. E, 2015, **92**, 053103.

38 C. Dutouquet, S. Acquaviva and J. Hermann, Spectrochim. Acta Part B, 2001, **56**, 629–635.

39 A. T. Patrascu, S. N. Yurchenko and J. Tennyson, Mon. Not. R. Astron. Soc., 2015, **449**, 3613–3619.

40 C. G. Parigger, A. C. Woods, D. M. Surmick, G. Gautam, M. J. Witte and J. O. Hornkohl, Spectrochimica Acta Part B: Atomic Spectroscopy, 2015, **107**, 132–138.

41 M. Dong, X. Mao, J. J. Gonzalez, J. Lu and R. E. Russo, Anal. Chem., 2013, **85**, 2899–2906.

42 Y. Huang, G. A. Risha, V. Yang and R. A. Yetter, Combust. Flame, 2009, **156**, 5–13.

43 O. Varenne, P.-G. Fournier, J. Fournier, B. Bellaoui, A.-I. Faké, J. Rostas and G. Taßeb, Nucl. Inst. Methods Phys. Res. B, 2000, **171**, 259–276.

44 K. Kasatani, H. Higashide, H. Shinohara and H. Sato, Chem. Phys. Lett., 1990, **174**, 71–74.

45 J. Lam, D. Amans, F. Chaput, M. Diouf, G. Ledoux, N. Mary, K. Masenelli-Varlot, V. Motto-Ros and C. Dujardin, Phys. Chem. Chem. Phys., 2014, **16**, 963–973.

46 T. Sakka, K. Saito and Y. H. Ogata, J. Appl. Phys., 2005, **97**, 014902.

47 K. Saito, T. Sakka and Y. H. Ogata, J. Appl. Phys., 2003, **94**, 5530–5536.